

Ferromagnetic Ordering in CeZnSn

Wilfried Hermes^a, Samir F. Matar^b, Thomas Harmening^a, Ute Ch. Rodewald^a, Matthias Eul^a, and Rainer Pöttgen^a

^a Institut für Anorganische und Analytische Chemie and NRW Graduate School of Chemistry, Universität Münster, Corrensstraße 30, D-48149 Münster, Germany

^b CNRS, Université de Bordeaux, ICMCB, 87 Avenue du Docteur Albert Schweitzer, F-33608 Pessac Cedex, France

Reprint requests to R. Pöttgen. E-mail: pottgen@uni-muenster.de

Z. Naturforsch. **2009**, *64b*, 175 – 183; received November 11, 2008

Dedicated to Professor Ingo-Peter Lorenz on the occasion of his 65th birthday

The stannide CeZnSn was obtained in X-ray-pure form by induction-melting of the elements in a sealed tantalum ampoule. CeZnSn crystallizes with the YPtAs-type structure, space group $P6_3/mmc$, $a = 456.7(3)$, $c = 1673.8(5)$ pm, $wR2 = 0.0862$, 259 F^2 values, and 12 variables. The zinc and tin atoms build up puckered Zn_3Sn_3 hexagons (Zn–Sn 271 pm) with weak interlayer Zn–Zn interactions (323 pm). Susceptibility measurements of CeZnSn reveal modified Curie-Weiss behavior above 50 K with an experimental magnetic moment of $2.77(1) \mu_B / \text{Ce atom}$. The cerium magnetic moments order ferromagnetically at $T_C = 5.2(1)$ K. ^{119}Sn Mössbauer spectra show a single tin site at an isomer shift of $\delta = 1.967(4)$ mm/s subjected to a small quadrupole splitting of $\Delta E_Q = 0.41(2)$ mm/s at 40 K. At 4.2 K a magnetic hyperfine field of $0.872(5)$ T is transferred to the tin site. From DFT scalar relativistic calculations of the electronic and magnetic structures, chemical bonding analysis reveals on one hand a weaker bonding of Zn than of Sn with the cerium substructures with a twice stronger Ce1–Sn bond compared to Ce2–Sn. On the other hand, a ferromagnetic ground state is identified from total energy differences in agreement with experiment.

Key words: Intermetallics, Stannide, Crystal Chemistry, Chemical Bonding (COOP), DFT, Spin Polarized Calculations, DOS, ELF

Introduction

Most of the equiatomic intermetallic cerium compounds $\text{Ce}TX$ (T = late transition metal; X = element of the 3rd, 4th, or 5th main group) crystallize either with the hexagonal ZrNiAl-type structure [1–3], or with AlB_2 -related superstructures [4] which consist of networks of ordered T_3X_3 hexagons. The simplest ordering variant for the $\text{Ce}TX$ compounds is the ZrBeSi type [5], where the T_3X_3 hexagons are rotated around the hexagonal axis by 60° in every other layer. Prominent examples for this structural arrangement are the antimonide CeNiSb [6] or the germanide CeCuGe [7] with planar Ni_3Sb_3 and Cu_3Ge_3 nets, respectively.

Similar atomic arrangements occur for the NdPtSb-type [8] compounds CeAuGe [9] and CeAuSn [10, 11], which consist of slightly puckered Au_3Ge_3 and Au_3Sn_3 hexagons. Most $\text{Ce}TX$ representatives in the AlB_2 -related structural family adopt the orthorhombic TiNiSi-type structure [12]. These $\text{Ce}TX$ structures

show strong tilts of the T_3X_3 hexagons and often large deviations from the hexagonal subcell symmetry. Variations of the lattice parameters and the free structural parameters (all atoms are on Wyckoff sites $4c: x \ 1/4 \ z$) allow a high flexibility for this structure type, allowing for various patterns of chemical bonding [13, 14]. A literature overview on the many TiNiSi-type phases is given in refs. [15–17]. The germanides CePdGe [18] and CePtGe [19] form superstructures related to the TiNiSi type with tripling or doubling of the subcells. This superstructure formation is driven by the formation of weak interlayer Pd–Pd and Pt–Pt interactions.

In the hexagonal branch of the AlB_2 -related superstructures, the stannide CeZnSn [20] has also been reported. The published structural data were based on a Rietveld refinement. CeZnSn has a pronounced AlB_2 -type subcell, but superstructure reflections require a quadrupled c axis. The structure consists of puckered Zn_3Sn_3 hexagons with weak interlayer Zn–Zn interactions. In the course of our systematic structure-

property investigations of CeTX intermetallics we have become interested in the magnetic behavior of CeZnSn which contains two crystallographically independent cerium sites. Herein we report on a single crystal study, electronic structure calculations, the magnetic properties and ^{119}Sn Mössbauer spectroscopy of CeZnSn.

Experimental Section

Synthesis

Starting materials for the preparation of CeZnSn were a cerium ingot (Johnson-Matthey), and zinc and tin granules (Merck), all with stated purities better than 99.9%. Pieces of the cerium ingot were first arc-melted [21] to a small button under an argon atmosphere. The argon was purified before with molecular sieves, silica gel, and titanium sponge (900 K). Subsequently, the cerium button and pieces of the zinc and tin granules were weighed in the ideal 1 : 1 : 1 atomic ratio and arc-welded in a small tantalum ampoule under an argon pressure of 700 mbar. The ampoule was then placed in a water-cooled sample chamber [22] of an induction furnace (Hüttinger Elektronik, Freiburg, Germany; type TIG 5/300) and three times heated for 5 min at 1360 K. After the third step the sample was kept at 1360 K for 10 min, rapidly cooled to 920 K, and subsequently annealed at that temperature for another 6 h. Finally the tube was quenched to r. t. by switching off the power of the generator. The brittle CeZnSn sample could readily be separated from the tantalum tube by mechanical fragmentation. No reaction with the crucible material was evident. CeZnSn is stable in air over several weeks. Single crystals exhibit metallic lustre while ground powder is dark grey.

EDX data

Semiquantitative EDX analyses of the crystal investigated on the diffractometer were carried out with a Leica 420i scanning electron microscope with CeO₂, Zn, and Sn as standards. The experimentally observed composition was close to the equiatomic one. No impurity elements heavier than sodium (detection limit of the instrument) were found.

X-Ray diffraction

The polycrystalline CeZnSn sample was characterized through X-ray powder diffraction (Guinier technique, imaging plate detector, Fujifilm BAS-1800) with CuK α_1 radiation and α -quartz ($a = 491.30$, $c = 540.46$ pm) as an internal standard. The hexagonal lattice parameters (Table 1) were refined from the Guinier data by a least-squares routine. The correct indexing was ensured by an intensity calculation [23]. Our data are in agreement with powder data published by Manfrinetti *et al.* ($a = 456.5(1)$, $c = 1670.8(2)$ pm) [20].

Table 1. Crystal data and structure refinement for CeZnSn (space group $P6_3/mmc$, $Z = 4$).

	CeZnSn
Empirical formula	CeZnSn
Formula weight, g mol ⁻¹	324.18
Unit cell dimensions (Guinier powder data)	
a , pm	456.7(3)
c , pm	1673.8(5)
V , nm ³	0.3023
Calculated density, g cm ⁻³	7.12
Crystal size, μm^3	20 × 30 × 60
Transm. ratio (max/min)	3.82
Absorption coefficient, mm ⁻¹	30.5
$F(000)$, e	552
θ range for data collection, deg	4–33
Range in hkl	±6; ±6; ±25
Total no. reflections	14619
Independent reflections / R_{int}	259 / 0.0564
Reflections with $I \geq 2\sigma(I)/R_\sigma$	187 / 0.0127
Data / parameters	259 / 12
Goodness-of-fit on F^2	1.071
Final $R1/wR2$ indices [$I \geq 2\sigma(I)$]	0.0296 / 0.0758
Final $R1/wR2$ indices (all data)	0.0502 / 0.0862
Extinction coefficient	0.0014(6)
Largest diff. peak / hole, e Å ⁻³	4.55 / -3.31

Small irregularly shaped single crystals of CeZnSn were selected from the crushed sample. Their quality was tested by Laue photographs on a Buerger camera using white Mo radiation. Intensity data were collected on a Stoe IPDS II diffractometer (graphite-monochromatized MoK α radiation; oscillation mode). A numerical absorption correction was applied to the data set. All relevant details concerning the data collection and evaluation are listed in Table 1.

Structure refinement

X-ray powder data of CeZnSn were already available from the Rietveld refinement performed by Manfrinetti *et al.* [20]. In perfect agreement with these investigations, space group $P6_3/mmc$ was found to be the correct one. The atomic positions from reference [20] were used as starting parameters, and the structure was refined using SHELXL-97 [24] (full-matrix least-squares on F^2) with anisotropic atomic displacement parameters for all atoms. As a check for possible mixed occupied sites, all occupancy parameters were refined in separate series of least-squares cycles. Since all sites were fully occupied within two standard deviations, the ideal occupancies were assumed again in the final cycles. The final difference Fourier synthesis was flat (Table 1). The positional parameters and interatomic distances are listed in Tables 2 and 3.

Further details of the crystal structure investigation may be obtained from Fachinformationszentrum Karlsruhe, 76344 Eggenstein-Leopoldshafen, Germany (fax: +49-7247-808-666; e-mail: crysdata@fiz-karlsruhe.de, http://www.fiz-informationsdienste.de/en/DB/icsd/depot_anforderung.html) on quoting the deposition number CSD-420050.

Table 2. Atomic coordinates and anisotropic displacement parameters (pm^2) for CeZnSn. U_{eq} is defined as one third of the trace of the orthogonalized U_{ij} tensor. The anisotropic displacement factor exponent takes the form: $-2\pi^2[(ha^*)^2U_{11} + \dots + 2hka^*b^*U_{12}]$. $U_{13} = U_{23} = 0$; $U_{12} = 1/2U_{11}$.

Atom	Wyckoff position	x	y	z	$U_{11} = U_{22}$	U_{33}	U_{eq}
Ce1	2a	0	0	0	75(4)	84(4)	78(3)
Ce2	2b	0	0	1/4	66(4)	74(4)	68(3)
Zn	4f	1/3	2/3	0.15364(12)	77(5)	255(10)	137(4)
Sn	4f	1/3	2/3	0.61691(6)	58(3)	100(4)	72(3)

Table 3. Interatomic distances (pm) in CeZnSn, calculated with the powder lattice parameters. Standard deviations are all equal or smaller than 0.2 pm. All distances within the first coordination spheres are listed.

Ce1:	6	Sn	328.4	Zn:	3	Sn	270.8
	6	Zn	368.3		3	Ce2	309.1
	2	Ce2	418.5		1	Zn	322.6
	6	Ce1	456.7		3	Ce1	368.3
Ce2:	6	Zn	309.1	Sn:	3	Zn	270.8
	6	Sn	345.2		3	Ce1	328.4
	2	Ce1	418.5		3	Ce2	345.2
	6	Ce2	456.7				

Physical property measurements

30.175 mg of the CeZnSn sample was packed in kapton foil and attached to the sample holder rod of a VSM for measuring the magnetic properties in a Quantum Design Physical-Property-Measurement-System in the temperature range 2.1–305 K with magnetic flux densities up to 80 kOe. For heat capacity (C_p) measurements (2.1–200 K), 11.182 mg of CeZnSn was glued to the platform of a pre-calibrated heat capacity puck using *Apiezon N grease*.

A $\text{Ca}^{119\text{m}}\text{SnO}_3$ source was available for the ^{119}Sn Mössbauer spectroscopic investigations. The sample was placed within thin-walled PVC containers at a thickness of about 10 mg Sn cm^{-2} . A palladium foil of 0.05 mm thickness was used to reduce the tin K X-rays concurrently emitted by this source. The measurements were conducted in the usual transmission geometry at 40 and 4.2 K.

Computational framework

The electronic structure calculations were performed within the density functional theoretical (DFT) framework [25] using the scalar relativistic augmented spherical wave (ASW) method [26]. All valence states, including the 4f (Ce) orbitals, were treated as band states. In the minimal ASW basis set, the outermost shells were chosen to represent the valence states using partial waves up to $l_{\text{max}} + 1 = 4$ for Ce, $l_{\text{max}} + 1 = 3$ for Zn and Sn. From preliminary calculations assuming Zn $3d^{10}$ states as part of the valence band, these states were found strongly localized at low energy ($\sim -8 \text{ eV}$) with a filling close to 10 electrons, meaning that they do not intervene in the chemical bonding. This led us to

consider them as core states in the subsequent calculations. The completeness of the valence basis set was checked for charge convergence, *i. e.* less than 0.1 electron for $l_{\text{max}} + 1$. The self-consistent field calculations were run to a convergence of 10^{-8} for the charge density. The accuracy of the method is in the range of about 10^{-8} Ryd regarding energy differences. Exchange and correlation effects were accounted for using the local density approximation (LDA) scheme of Vosko, Wilk and Nusair [27]. In as far as the experimental lattice and positional parameters (above) are used as only inputs with neutral atomic species, the calculations are *ab initio*. They are conducted self-consistently within the charge and energy difference criteria defined before. The Brillouin zone integrations were performed using a linear tetrahedron method for k-points integration (up to 1000 points) within the irreducible wedge of the hexagonal Bravais lattice [28].

Firstly, spin-degenerate non-spin polarized (NSP) calculations were carried out. Assuming a non-magnetic configuration means that the spin degeneracy is enforced for all species. Then spin polarized (SP) calculations were done for a long range ferromagnetic (SP/F) order. However, for a check of the actual ground state further antiferromagnetic (SP/AF) calculations were also done by allowing each substructure to be half UP spins and half DOWN spins. The ground state was thus determined from energy differences between the magnetic configurations. To extract more information about the nature of the interactions between the atomic constituents from electronic structure calculations, the covalent bond energy criterion ECOV [29] was observed, merging both the crystal orbital Hamiltonian population (COHP) and crystal orbital overlap population (COOP) to calculate quantities independent of the particular choice of the potential zero. In the plots, negative, positive and zero magnitudes of ECOV are indicative of bonding, antibonding, and nonbonding interactions, respectively. We also carried out an analysis in the real space of the electron localization using the electron localization function (ELF) [30]. It allows to determine the amount of localization of electrons with respect to the free electron gas distribution. This normalization provides a dimensionless ELF magnitude ranging from 0 to 1, with $\text{ELF} = 1/2$ corresponding to the free electron gas distribution. These three extreme situations are illustrated by three sets of colors: $\text{ELF} = 0$ points to no local-

ization (blue contours), $ELF = 1$ indicates strong localization (red contours), and $ELF = 1/2$, with green contours, is relevant to nearly free electron like behavior (*vide infra*).

Discussion

Crystal chemistry

The present single crystal data on CeZnSn confirm the Rietveld refinement by Manfrinetti and Pani [20], however, the positional parameters have much higher precision. A view of the unit cell is presented in Fig. 1. Since the crystal chemistry of the YPtAs-related phases has already been discussed in a review article [4] and together with the structure of isotypic UAuGe [31], here we concentrate only on the structural peculiarities of CeZnSn. As emphasized in Fig. 1, the zinc and tin atoms build up puckered Zn_3Sn_3 hexagons with Zn–Sn distances of 271 pm. The latter are only slightly longer than the sum of the covalent radii [32] of 265 pm. In the distorted tetrahedral [ZnSn] network of EuZnSn [33] the Zn–Sn distances are even longer (278–305 pm).

Although the Zn_3Sn_3 layers in CeZnSn have all the same composition, they have different orientation and puckering, resulting in the stacking sequence A B B' A'. This results in Zn–Zn interlayer interactions be-

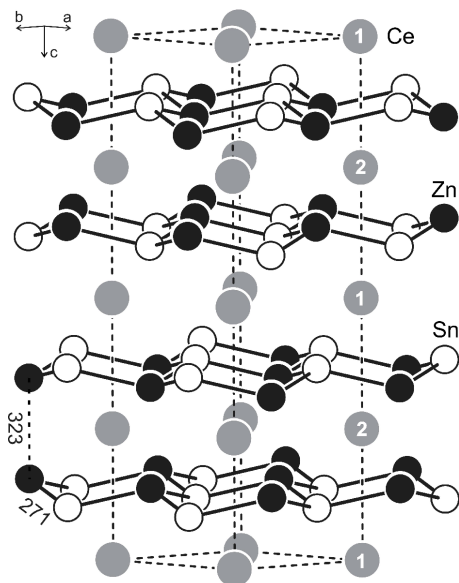


Fig. 1. The crystal structure of CeZnSn. Cerium, zinc, and tin atoms are drawn as light grey, black filled, and open circles, respectively. The puckered Zn_3Sn_3 hexagons, relevant interatomic distances, and the crystallographically independent cerium sites are indicated.

tween the layers A and B and B' and A' (Fig. 1). However, due to the electron configuration of Zn ($3d^{10}4s^2$), the filled d states lying at low energy are not expected to play an important role in the chemical bonding, and non-directional s -like states are likely to show free electron-like features; this is discussed in the electronic structure section. The Zn–Zn distances of 323 pm, however, are much longer than in *hcp* zinc where each zinc atom has six neighbors at 266 and six further neighbors at 291 pm [34]. These interlayer interactions can only be considered as weak, however, they might be the key for the superstructure formation.

The related compound EuZnSn [33] contains stable divalent europium [35], and consequently a valence-precise Zintl formulation $Eu^{2+}Zn^{2+}Sn^{4-}$ can be applied, in agreement with the isolated tin atoms. This is different in CeZnSn discussed herein. The magnetic susceptibility data (*vide infra*) clearly point to a trivalent state for both cerium sites. Consequently a Zintl-type formulation $Ce^{3+}Zn^{2+}Sn^{4-}e^-$ leaves one excess electron. This peculiar bonding situation is addressed in more detail by electronic structure calculations in the following chapter.

Electronic structure and chemical bonding analyses

NSP calculations

Density of states (DOS) and magnetic instability

The site-projected PDOS are shown in Fig. 2. In this plot as well as in the following ones the zero

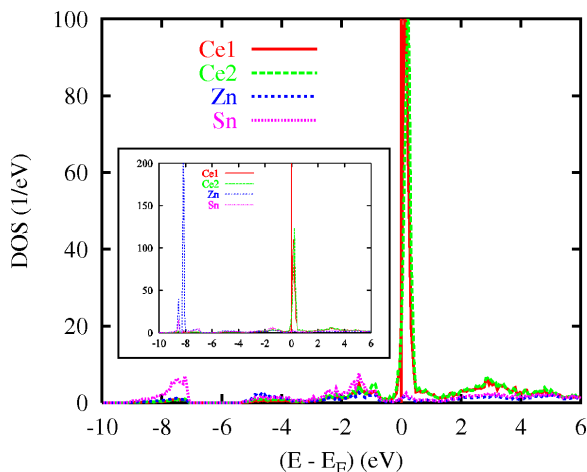


Fig. 2 (color online). Non-magnetic CeZnSn: site projected density of states; the inset shows the low-lying Zn-3d states below -8 eV. Zero energy is with respect to the Fermi level E_F .

energy along the x axis is with respect to the Fermi level E_F . At E_F the major feature is the crossing at a relatively large intensity of the Ce $4f$ states, $n(E_F)_{\text{Ce1}} = 9.56 \text{ eV}^{-1}$ and $n(E_F)_{\text{Ce2}} = 8.38 \text{ eV}^{-1}$, while the Ce $4f$ band is mainly found and centered within the conduction band CB due to the low filling of the $4f$ states. Such a result can be analyzed within the Stoner mean field theory of band ferromagnetism [36, 37] which predicts the system to be unstable in a non-magnetic state if it is characterized by a large $n(E_F)$. This is expressed by the unitless Stoner product: $I \cdot n(E_F)$ which can be either larger or smaller than 1 depending on whether the system will be unstable in a spin-degenerate, non-magnetic configuration or not, respectively. The term I is the Stoner integral obtained from a spin-polarized calculation of the relevant constituent, here cerium. From previous investigations on uranium- and cerium-containing magnetic intermetallic systems [37], $I(\text{Ce}) = 0.272 \text{ eV}$. The resulting Stoner products are then 2.58 and 2.28 for Ce1 and Ce2, respectively. Thus due to large Stoner products the system is expected to magnetically polarize, *i. e.*, cerium at both sites will carry a finite magnetic moment due to $4f$ band polarization. The Ce1–Ce1/Ce2–Ce2/Ce1–Ce2 distances (456.7/456.7/418.5 pm) are all above the critical Hill limit [38] of about 340 pm for f electron localization, so that sufficient localization for the onset of ordered magnetic moments can be expected.

Below E_F the itinerant states are found for all species. They show similar peak structures featuring chemical bonding in this energy region as it is discussed below. At $\sim -8 \text{ eV}$ and below the s states of Sn and Zn are found; they are expected to play little role in the bonding as shown below.

Chemical bonding analysis

Chemical bonding properties can be addressed on the basis of the spin-degenerate calculations. This is due to the fact that the spin-polarized electronic bands, to a large extent, result from the spin-degenerate bands by a rigid spin splitting. Fig. 3 shows the unit-less ECOV for the different interactions within CeZnSn. The energy window around E_F has been reduced to the $\pm 4.4 \text{ eV}$ range because most of the bonding occurs in this energy region as already discussed in the DOS section. The VB is bonding altogether (negative ECOV magnitudes), and one can notice different behavior of the Zn and Sn substructures

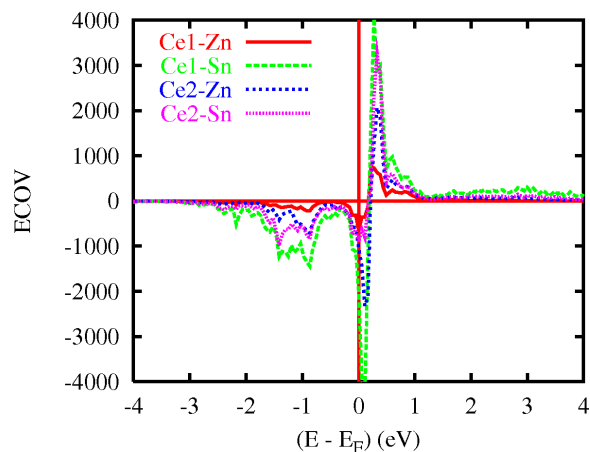


Fig. 3 (color online). Non-magnetic CeZnSn: chemical bonding based on the ECOV criterion (*cf.* text). Zero energy is with respect to the Fermi level E_F .

tures with Ce1 and Ce2. The strongest interaction occurs for the Sn substructure with a twice stronger Ce1–Sn bond with respect to Ce2–Sn. Weaker bonding is found for the Zn substructure where the Ce2–Zn bond is the strongest. One could firstly suggest this bonding behavior to follow from the respective distances (in pm): $d(\text{Ce1–Sn})/d(\text{Ce2–Sn}) = 328/345$ and $d(\text{Ce1–Zn})/d(\text{Ce2–Zn}) = 368/309$. While these distances follow the strength of the bonding this cannot explain the weakness of the Zn substructure bonding with Ce1 and Ce2. This actually pertains to the fact that contrary to Sn which has $5s$ and $5p$ states in the valence basis set, there are only $4s$ states (full $3d$ states not involved with the bonding) for Zn which somehow makes this atom to behave as an alkaline earth element such as Ca ($4s^2$). Then the loss of directional p orbitals weakens the bonding of Zn with Ce as well as with Sn, despite a relatively short Sn–Zn separation of 271 pm.

Mapping of the electron localization

The chemical bonding observations can be further illustrated by the mapping of the electron localization using the ELF normalized function presented above. The slice plane in Fig. 4 shows the strong localization around Sn; a distortion of electron distribution (half moon-shape of red contours) can be related to the Sn s^2 lone pairs. By contrast, Zn shows no localization and the non-directional s states between atoms show free electron-like features (green areas). From this the system can be labeled as a stannide from the

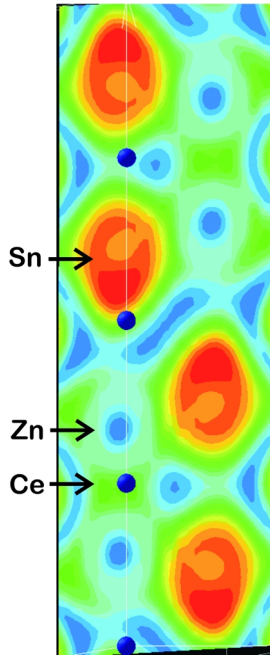


Fig. 4 (color online). ELF of CeZnSn approximately showing the [110] plane crossing the zinc and tin sites (*cf.* Fig. 1 and text). The cerium atoms are also shown for clarity.

chemistry standpoint although the calculations do not exhibit features of ionized species. This is also made clear from the vertical planes (along 001) crossing the Zn–Sn chains (Fig. 1).

Spin-polarized calculations

From the NSP calculations and their analysis within the Stoner mean field theory of band ferromagnetism, it has been established that the CeZnSn system is unstable in this model configuration due to the large $n(E_F)$ of both Ce substructures. Consequently, spin-polarized calculations were carried out, assuming implicitly a hypothetical ferromagnetic order, in agreement with the magnetic properties discussed below. At self consistency the relative energy difference with respect to the non-magnetic (NSP) energy, $\Delta E(\text{SP/F-NSP})$ is $-0.1084 \text{ eV}\cdot\text{fu}^{-1}$ (fu: formula unit CeZnSn). The spin only magnetic moments are carried by Ce as expected, with $M(\text{Ce1}) = 0.831 \mu_B$ and $M(\text{Ce2}) = 0.889 \mu_B$ and $M(\text{fu}) = 0.86 \mu_B$. The slightly larger moment carried by Ce2 arises from its stronger interaction with Zn leading to a larger f population. Note that the occupation of Ce ($4f$) ~ 1.3 electrons gives rise to an orbital moment of $\sim 2.5 \mu_B$ of opposite sign to the spin moment (Hund's

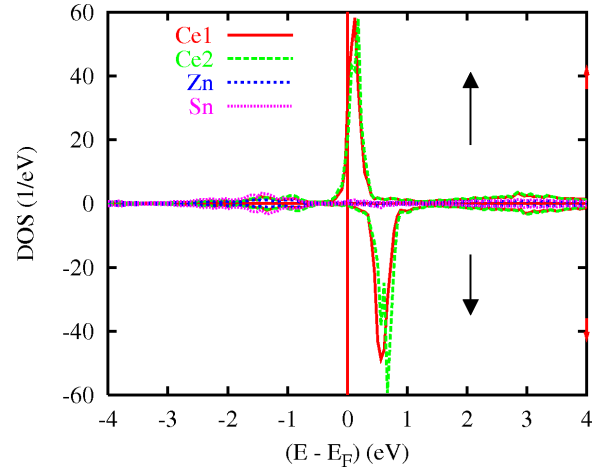


Fig. 5 (color online). Spin polarized ferromagnetic site projected density of states of CeZnSn showing the polarization of both cerium sites. Low energy lying s states are not shown. Zero energy is with respect to the Fermi level E_F .

3rd rule) – *cf.* [37] and references therein. Fig. 5 shows the site- and spin-projected DOS for SP/F CeZnSn; Sn/Zn s states at -10 eV are not shown. Clearly exchange splitting between majority (\uparrow) and minority (\downarrow) spin populations affects the cerium substructures which show slightly different peak shapes: the Ce1 PDOS tends to be broader than the Ce2 one due to the overall stronger mixing with Sn/Zn (*cf.* Fig. 3). The other parts of the VB in the energy range $-3, -1$ are not changed energetically with respect to the NSP calculations.

Lastly, a hypothetical SP-AFM configuration is assumed by splitting the respective substructure of Ce1(twofold), Ce2(twofold), Zn(fourfold) and Sn(fourfold) into half UP spins and half DOWN spins. However, this configuration turns out to be energetically less stable: $\Delta E(\text{SP/AF-SP/F}) = +0.012 \text{ eV}\cdot\text{fu}^{-1}$. The experimental findings point to ferromagnetic ordering at low temperature (*vide infra*) so that our calculational results are in good agreement with the experiment.

Magnetic behavior and ^{119}Sn Mössbauer spectroscopy

CeZnSn is one of the rare examples of intermetallic CeTX compounds with two crystallographically independent cerium sites. The recently reported zinc compound CeRhZn [39] contains two cerium sites with almost tetravalent cerium. In the stannide

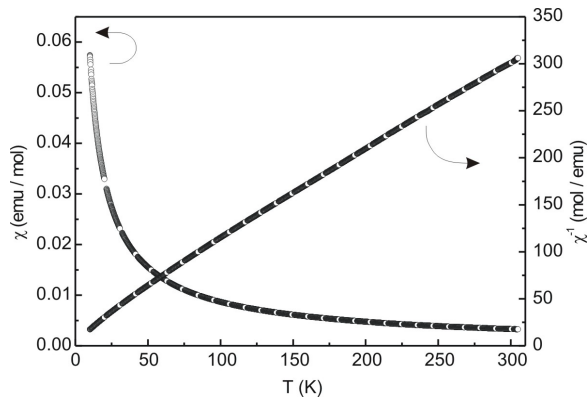


Fig. 6. Temperature dependence of the magnetic susceptibility (χ and χ^{-1} data) of CeZnSn measured at 40 kOe.

CeRuSn [17, 40] one of the cerium sites is trivalent and the second one is intermediate-valent. In CeZnSn described herein, both cerium sites show a stable trivalent ground state.

The temperature dependence of the magnetic susceptibility (χ and χ^{-1} data) measured at 4 T is displayed in Fig. 6. Above 50 K, $\chi^{-1} = f(T)$ was analyzed using the modified Curie-Weiss expression $\chi^{-1} = 1/[\chi_0 + C/(T - \theta_p)]$ where θ_p is the asymptotic Curie temperature, C is the Curie constant and χ_0 includes the temperature-independent Van Vleck correction, the diamagnetic core correction and the paramagnetic contribution of the conduction electrons. The values of θ_p , χ_0 and $\mu_{\text{eff}} = (8C)^{1/2} \mu_B$ were refined by a least-squares method giving $\theta_p = -14.6(1)$ K, $\chi_0 = 2.2 \cdot 10^{-4}$ emu mol $^{-1}$ and $\mu_{\text{eff}} = 2.77(1) \mu_B/\text{Ce atom}$ for CeZnSn. The experimental effective magnetic moment is slightly higher than that of the free ion value with $\mu_{\text{theo}} = 2.54 \mu_B/\text{Ce}^{3+}$. This must be due to a relatively strong interaction of Ce2 with zinc as mentioned above (*spin polarized calculations*). Below 15 K, χ increases strongly, indicating ferromagnetic ordering in the low-temperature region.

The exact Curie temperature was determined from a kink-point measurement (Fig. 7). We have therefore measured the susceptibility in a low external field of 100 Oe in the zero-field-cooling and in the field-cooling mode. The derivative $d\chi/dT$ of the zero-field-cooling measurement resulted in a Curie temperature of $T_C = 5.2(1)$ K.

The magnetization isotherms taken at 4 and 50 K are shown in Fig. 8. At 50 K we observe an almost linear increase of the magnetization with the applied

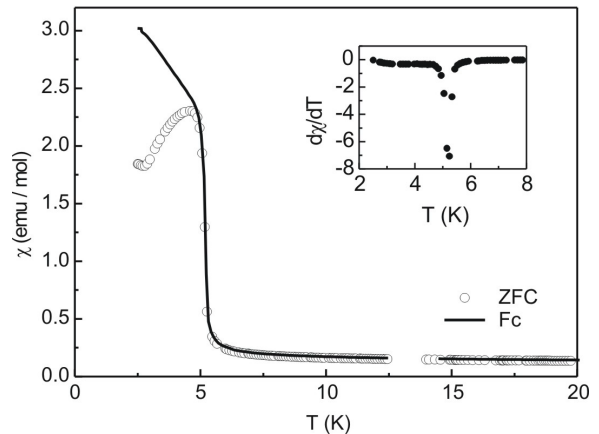


Fig. 7. Low-temperature susceptibility (zero-field-cooling and field-cooling modus) of CeZnSn at 100 Oe (kink-point measurement). The inset shows the derivative $d\chi/dT$ of the zero-field-cooling curve with a sharp peak at the Curie temperature of $T_C = 5.2$ K.

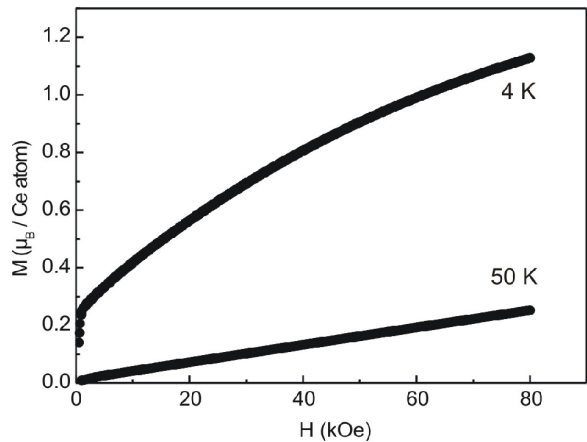


Fig. 8. Magnetization isotherms of CeZnSn measured at 4 and 50 K.

field as expected for a paramagnetic material. In contrast, at 4 K, only slightly below the Curie temperature, the magnetization increases steeply up to an external field strength of 0.1 T, and above 0.1 T the curvature becomes more pronounced and shows a tendency for saturation at high fields. The saturation magnetization (m) at 80 kOe amounts to $\mu_{\text{exp}(sm)} = 1.13(1) \mu_B/\text{Ce atom}$, significantly reduced from the theoretical one for Ce^{3+} at $2.14 \mu_B/\text{Ce atom}$. Saturation moments in the range of $1 \mu_B/\text{Ce atom}$ are frequently observed for similar ternary intermetallics, *e. g.* CeNiIn $_2$ [41] or CeRhSn $_2$ [42]. These small values of the saturation are due to crystal field splitting effects on the $J = 5/2$ ground state of the Ce^{3+} ion. In Fig. 9

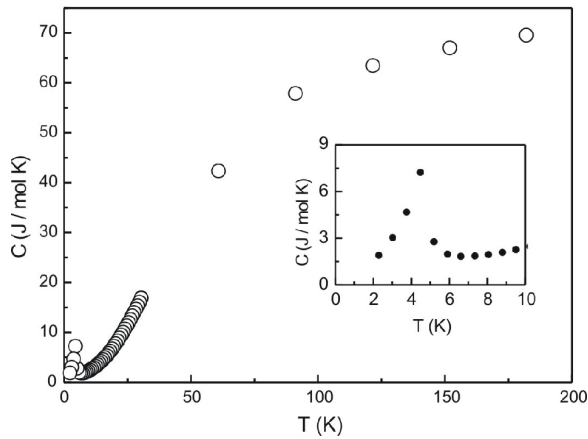


Fig. 9. Temperature dependence of the specific heat of CeZnSn in zero magnetic field. The low-temperature behavior is shown in the inset.

the specific heat (C_p) data is plotted for CeZnSn. The Curie-Temperature of 5.2(1) K is characterized by a λ -like anomaly and is in good agreement with the kink-point measurement.

The ^{119}Sn Mössbauer studies of CeZnSn were performed at 40 and 4.2 K (Fig. 10 and Table 4). The non-cubic local symmetry at the tin sites ($3m.$) leads to resonance spectra with a non-vanishing quadrupole splitting. The spectrum at 40 K *i. e.*, in the paramagnetic range, was fitted as a typical quadrupole doublet. Because of the threefold symmetry axis, the asymmetry parameter $\eta = (V_{xx} - V_{yy})/V_{zz}$ is assumed to be zero. Then, the experimentally determined quadrupole splitting gives directly the absolute value of the quadrupole interaction constant $|\Delta E_Q|$. At 4.2 K a magnetic hyperfine field of 0.872(5) T is transferred to the tin nuclei due to ferromagnetic ordering of the cerium magnetic moments. The magnitude of the electric quadrupole interactions does not change, and the sign was found to be positive. This indicates the direction of transferred magnetic hyperfine field to be parallel to the principal axis of the electric field gradient.

Finally we compare the isomer shift of 1.97 mm s^{-1} for CeZnSn with the value obtained for the Zintl phase EuZnSn (1.94 mm s^{-1} at 78 K) [35]. The isomer shifts

Table 4. Fitting parameters of ^{119}Sn Mössbauer spectroscopic measurements for CeZnSn. Numbers in parentheses represent the statistical errors in the last digit. δ , isomer shift; ΔE_Q , electric quadrupole interaction; Γ , experimental line width; B_{hf} , magnetic hyperfine field.

T (K)	δ (mm s^{-1})	ΔE_Q (mm s^{-1})	Γ (mm s^{-1})	B_{hf} (T)
40	1.967(4)	0.41(2)	1.09(2)	–
4.2	1.977(3)	0.48(1)	1.03(1)	0.872(5)

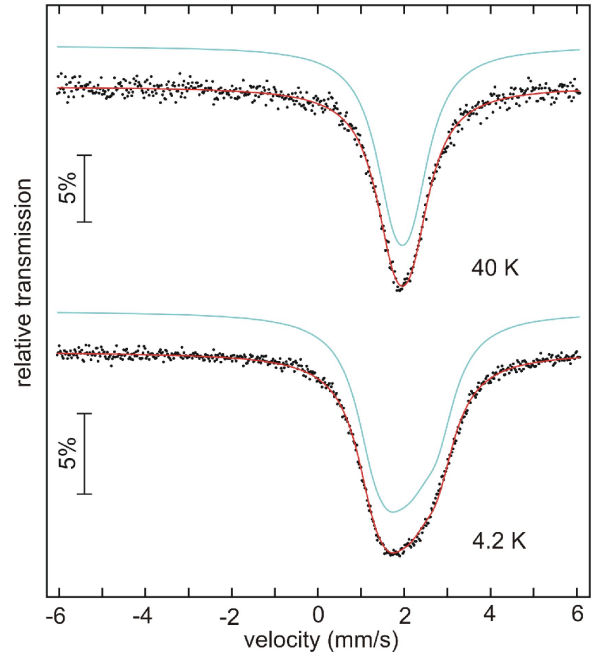


Fig. 10. Experimental (data points) and simulated (continuous line) ^{119}Sn Mössbauer spectra of CeZnSn at 40 and 4.2 K.

indicate similar electron density at the tin nuclei in both stannides.

Acknowledgements

This work was financially supported by the Deutsche Forschungsgemeinschaft. W.H. and T.H. are indebted to the Fonds der Chemischen Industrie and the NRW Graduate School of Chemistry for a PhD stipend. Computational facilities provided by the M3PEC-Mésocentre of University Bordeaux 1 are acknowledged.

- [1] P.I. Krypyakevich, V. Ya. Markiv, E. V. Melnyk, *Dopov. Akad. Nauk. Ukr. RSR, Ser. A* **1967**, 750.
- [2] A. E. Dwight, M. H. Mueller, R. A. Conner, Jr., J. W. Downey, H. Knott, *Trans. Met. Soc. AIME* **1968**, 242, 2075.
- [3] M. F. Zumdick, R.-D. Hoffmann, R. Pöttgen, *Z. Naturforsch.* **1999**, 54b, 45.
- [4] R.-D. Hoffmann, R. Pöttgen, *Z. Kristallogr.* **2001**, 216, 127.
- [5] J. W. Nielsen, N. C. Baenziger, *Acta Crystallogr.* **1954**, 7, 132.
- [6] K. Hartjes, W. Jeitschko, *J. Alloys Compd.* **1995**, 226, 81.
- [7] B. Chevalier, M. Pasturel, J.-L. Bobet, F. Weill, R. Decourt, J. Etourneau, *J. Solid State Chem.* **2004**, 177, 752.
- [8] G. Wenski, A. Mewis, *Z. Kristallogr.* **1986**, 176, 125.
- [9] R. Pöttgen, H. Borrmann, R. K. Kremer, *J. Magn. Magn. Mater.* **1996**, 152, 196.
- [10] D. Niepmann, R. Pöttgen, K. M. Poduska, F. J. DiSalvo, H. Trill, B. D. Mosel, *Z. Naturforsch.* **2001**, 56b, 1.
- [11] M. Lenkewitz, S. Corsépius, G. R. Stewart, *J. Alloys Compd.* **1996**, 241, 121.
- [12] C. B. Shoemaker, D. P. Shoemaker, *Acta Crystallogr.* **1965**, 18, 900.
- [13] G. Nussli, K. Polborn, J. Evers, G. A. Landrum, R. Hoffmann, *Inorg. Chem.* **1996**, 35, 6922.
- [14] G. A. Landrum, R. Hoffmann, J. Evers, H. Boysen, *Inorg. Chem.* **1998**, 37, 5754.
- [15] R. Kraft, R. Pöttgen, D. Kaczorowski, *Chem. Mater.* **2003**, 15, 2998.
- [16] B. Chevalier, B. Heying, U. Ch. Rodewald, C. P. Sebastian, E. Bauer, R. Pöttgen, *Chem. Mater.* **2007**, 19, 3052.
- [17] J. F. Riecken, W. Hermes, B. Chevalier, R.-D. Hoffmann, F. M. Schappacher, R. Pöttgen, *Z. Anorg. Allg. Chem.* **2007**, 633, 1094.
- [18] D. Niepmann, Yu. M. Protś, R. Pöttgen, W. Jeitschko, *J. Solid State Chem.* **2000**, 154, 329.
- [19] Yu. M. Protś, R. Pöttgen, D. Niepmann, M. Wolff, W. Jeitschko, *J. Solid State Chem.* **1999**, 142, 400.
- [20] P. Manfrinetti, M. Pani, *J. Alloys Compd.* **2005**, 393, 180.
- [21] R. Pöttgen, Th. Gulden, A. Simon, *GIT Labor-Fachzeitschrift* **1999**, 43, 133.
- [22] D. Kußmann, R.-D. Hoffmann, R. Pöttgen, *Z. Anorg. Allg. Chem.* **1998**, 624, 1727.
- [23] K. Yvon, W. Jeitschko, E. Parthé, *J. Appl. Crystallogr.* **1977**, 10, 73.
- [24] G. M. Sheldrick, SHELXL-97, Program for the Refinement of Crystal Structures, University of Göttingen, Göttingen (Germany) **1997**.
- [25] P. Hohenberg, W. Kohn, *Phys. Rev.* **1964**, 136, B864; W. Kohn, L. J. Sham, *Phys. Rev.* **1965**, 140, A1133.
- [26] A. R. Williams, J. Kübler, C. D. Gelatt, *Phys. Rev. B* **1979**, 19, 6094; V. Eyert, *The Augmented Spherical Wave Method – A. Comprehensive Treatment, Lect. Notes Phys.* Vol. 719, Springer, Berlin, Heidelberg **2007**.
- [27] S. H. Vosko, L. Wilk, M. Nusair, *Can. J. Phys.* **1980**, 58, 1200.
- [28] P. E. Blöchl, O. Jepsen, O. K. Anderson, *Phys. Rev. B* **1994**, 49, 16223.
- [29] G. Bester, M. Fähnle, *J. Phys.: Condens. Matter* **2001**, 13, 11541.
- [30] A. D. Becke, K. E. Edgecombe, *J. Chem. Phys.* **1990**, 92, 5397.
- [31] B. J. Gibson, R. K. Kremer, O. Jepsen, J. D. Garrett, R.-D. Hoffmann, R. Pöttgen, *J. Phys.: Condens. Matter* **2001**, 13, 3123.
- [32] J. Emsley, *The Elements*, Oxford University Press, Oxford **1999**.
- [33] R. Pöttgen, *Z. Kristallogr.* **1996**, 211, 884.
- [34] J. Donohue, *The Structures of the Elements*, Wiley, New York **1974**.
- [35] U. Ernet, R. Müllmann, B. D. Mosel, H. Eckert, R. Pöttgen, G. Kotzyba, *J. Mater. Chem.* **1997**, 7, 255.
- [36] J. Kübler, V. Eyert in *Materials Science and Technology*, Vol. 3A: *Electronic and Magnetic Properties of Metals and Ceramics*, Part I. (Ed.: K. H. J. Buschow), VCH-Verlag, Weinheim **1992**, p. 1–145.
- [37] S. F. Matar, A. Mavromaras, *J. Solid State Chem.* **2000**, 149, 449.
- [38] H. H. Hill in *Plutonium and other Actinides*, (Ed.: W. N. Mines) *Nuclear Materials Series*, AIME, **1970**, 17, 2.
- [39] W. Hermes, A. F. Al Alam, S. F. Matar, R. Pöttgen, *Solid State Sci.* **2008**, 10, 1895.
- [40] S. F. Matar, J. F. Riecken, B. Chevalier, A. F. Al Alam, V. Eyert, *Phys. Rev. B* **2007**, 76, 174434.
- [41] V. I. Zaremba, Ya. M. Kalychak, Yu. B. Tyvanchuk, R.-D. Hoffmann, M. H. Möller, R. Pöttgen, *Z. Naturforsch.* **2002**, 57b, 791.
- [42] D. Niepmann, R. Pöttgen, B. Künnen, G. Kotzyba, C. Rosenhahn, B. D. Mosel, *Chem. Mater.* **1999**, 11, 1597.